

Alternate current magnetic property characterization of nonstoichiometric zinc ferrite nanocrystals for inductor fabrication via a solution based process

Hongseok Yun, Jungkwun Kim, Taejong Paik, Lingyao Meng, Pil Sung Jo, James M. Kikkawa, Cherie R. Kagan, Mark G. Allen, and Christopher B. Murray

Citation: *Journal of Applied Physics* **119**, 113901 (2016); doi: 10.1063/1.4942865

View online: <http://dx.doi.org/10.1063/1.4942865>

View Table of Contents: <http://scitation.aip.org/content/aip/journal/jap/119/11?ver=pdfcov>

Published by the [AIP Publishing](#)

Articles you may be interested in

[The effect of precursor types on the magnetic properties of Y-type hexa-ferrite composite](#)

J. Appl. Phys. **117**, 17A507 (2015); 10.1063/1.4918690

[Electromagnetic properties of NiZn ferrite nanoparticles and their polymer composites](#)

J. Appl. Phys. **115**, 173905 (2014); 10.1063/1.4873235

[An X-ray absorption spectroscopy study of the inversion degree in zinc ferrite nanocrystals dispersed on a highly porous silica aerogel matrix](#)

J. Chem. Phys. **138**, 054702 (2013); 10.1063/1.4789479

[A facile approach to enhance the high temperature stability of magnetite nanoparticles with improved magnetic property](#)

J. Appl. Phys. **113**, 044314 (2013); 10.1063/1.4789610

[Enhanced magnetic properties of Dy³⁺ substituted Ni-Cu-Zn ferrite nanoparticles](#)

Appl. Phys. Lett. **100**, 042407 (2012); 10.1063/1.3679688



NEW Special Topic Sections

NOW ONLINE
Lithium Niobate Properties and Applications:
Reviews of Emerging Trends

AIP | Applied Physics Reviews

Alternate current magnetic property characterization of nonstoichiometric zinc ferrite nanocrystals for inductor fabrication via a solution based process

Hongseok Yun,¹ Jungkwun Kim,² Taejong Paik,^{3,4} Lingyao Meng,³ Pil Sung Jo,^{3,5} James M. Kikkawa,⁶ Cherie R. Kagan,^{1,2,3} Mark G. Allen,² and Christopher B. Murray^{1,3,a)}

¹Department of Chemistry, University of Pennsylvania, Philadelphia, Pennsylvania 19104, USA

²Department of Electrical and Systems Engineering, University of Pennsylvania, Philadelphia, Pennsylvania 19104, USA

³Department of Materials Science and Engineering, University of Pennsylvania, Philadelphia, Pennsylvania 19104, USA

⁴School of Integrative Engineering, Chung-Ang University, Seoul 06974, South Korea

⁵Complex Assemblies of Soft Matter, CNRS-SOLVAY-PENN UMI 3254, Bristol, Pennsylvania 19007-3624, USA

⁶Department of Physics and Astronomy, University of Pennsylvania, Philadelphia, Pennsylvania 19104, USA

(Received 16 November 2015; accepted 15 February 2016; published online 17 March 2016)

We investigate the ac magnetic behavior of solution processable, non-stoichiometric zinc ferrite nanocrystals with a series of sizes and zinc concentrations. Nearly monodisperse $Zn_xFe_{3-x}O_4$ nanocrystals ($x = 0-0.25$) with an average size ranging from 7.4 nm to 13.8 nm are synthesized by using a solvothermal method. All the nanocrystals are in a superparamagnetic state at 300 K, which is confirmed by Superconductive Quantum Interference Device magnetometry. Due to the doping of non-magnetic Zn^{2+} into A site of ferrite, the saturation magnetization of nanocrystals increases as the size and Zn concentration increases. The ac magnetic permeability measurements at radio frequencies reveal that the real part of the magnetic permeability of similarly sized ferrite nanocrystals can be enhanced by almost twofold as the Zn^{2+} doping level increases from 0 to 0.25. The integration of 12.3 nm $Zn_{0.25}Fe_{2.75}O_4$ nanocrystals into a toroidal inductor and a solenoid inductor prepared via a simple solution cast process yields a higher quality factors than air core inductors with the same geometries up to 5 MHz and 9 MHz, respectively, which is in the regime of the switching frequencies for the advanced integrated power converters. © 2016 AIP Publishing LLC.

[<http://dx.doi.org/10.1063/1.4942865>]

I. INTRODUCTION

Colloidal magnetic nanocrystals (NCs) have been studied extensively as new building blocks for direct current (dc) magnetic applications such as high density magnetic recording,¹⁻³ magnetoresistance,⁴⁻⁶ and magnetic sensors.⁷⁻⁹ Recently, their applications have been extended to alternating current (ac) applications including electromagnetic shielding,¹⁰⁻¹² inductors,¹³⁻¹⁹ transformers,²⁰⁻²² and hyperthermal cancer treatments.²³⁻²⁶ Among these, the use of magnetic NCs for miniaturized ac magnetic applications is particularly intriguing due to their superparamagnetic behavior²⁷ and tunable magnetic properties. In addition, NCs synthesized via high temperature decomposition processes are dispersible in volatile solvents such as hexane, octane, and toluene, which makes them suitable for solution based processes.

Solution based deposition processes have been adopted in the fabrication of several types of devices, including solar cells,²⁸⁻³¹ transistors,³²⁻³⁵ and flexible electronics,³⁶⁻³⁹ because of their low manufacturing cost, compatibility with high-throughput processes, and large-area coverage. In particular, the scalable thickness and mild processing condition of the solution based processes make the techniques attractive to the production of flexible and miniaturized electromagnetic

devices such as microelectromechanical systems (MEMS). MEMS have been studied for miniaturizing inductors,⁴⁰⁻⁴² which are among the most widely used components in electro-devices, for example, power converters,^{43,44} wireless chargers,⁴⁵⁻⁴⁷ and inductive sensors.^{42,48} Miniaturization of inductors is possible by increasing the operating frequency of the inductors, which reduces the required inductance level.⁴⁹ However, the high magnetic energy loss (e.g., hysteresis loss and eddy current loss) of the conventional magnetic materials precludes the increase in the operating frequency.⁵⁰ Since the solution based fabrication processes allow a high degree of freedom in device designs and the magnetic properties of NCs can be tunable, we will exploit colloidal NCs as the magnetic core materials in miniature inductors.

To adopt colloidal magnetic NCs in ac magnetic applications with low energy loss, it is necessary to analyze their ac magnetic permeability, ferromagnetic resonance (FMR) frequency, coercivity, and electrical conductivity at high magnetic frequencies.⁵⁰⁻⁵² Since the magnetic permeability,^{16,17} FMR frequency,⁵³⁻⁵⁶ saturation magnetization,⁵⁷⁻⁵⁹ and coercivity^{17,26} of NCs are strongly dependent on the size, shape, and composition of NCs, it is particularly important to synthesize NCs with precisely controlled size and composition to understand the properties of NCs and devices fabricated from these. Zinc ferrites NCs are one of the most promising candidates because of their intrinsically high saturation magnetization and low magnetocrystalline anisotropy

^{a)}Author to whom correspondence should be sent. Electronic mail: cbmurray@sas.upenn.edu

energy.²⁶ Also, the insulating layer of organic ligands surrounding the colloidal NCs serve to suppress eddy currents, which are significant sources of energy loss in conventional magnetic materials. Though there are studies that motivate the interest in the magnetic permeability of zinc ferrite NCs,^{60–62} there has not been a systematic study which addresses both controlled NC size and composition. We use the insights gained to design ac devices based on zinc ferrite NCs operating at radio frequencies.

Here, we report the ac magnetic permeability of non-stoichiometric zinc ferrite NCs in radio frequency range. Spherical superparamagnetic $Zn_xFe_{3-x}O_4$ ($0 \leq x \leq 0.25$) NCs with precisely controlled sizes, narrow size distribution ($< 7\%$ by TEM images), and compositions are synthesized to investigate their size and composition dependent ac magnetic behavior. These superparamagnetic NCs are further analyzed by a one-turn inductor model for ac magnetic characterization from 1 MHz to 500 MHz. Finally, as a proof of concept, inductors with zinc ferrite NC cores are prepared via a simple solution drop-casting process and their inductances, resistances, and quality factors are measured.

II. EXPERIMENTAL METHODS

A. Materials

Zinc (II) acetylacetonate, iron (III) acetylacetonate (99+%), and 1-octadecene (technical grade, 90%) were purchased from Acros Organics. Oleic acid (technical grade, 90%) and oleylamine (technical grade, 70%) were purchased from Sigma-Aldrich. All the chemicals were used as received.

B. Synthesis of $Zn_{0.25}Fe_{2.75}O_4$ nanocrystals

For the synthesis of 8.3 nm $Zn_{0.25}Fe_{2.75}O_4$ NCs, 6 mmol of zinc (II) acetylacetonate, 12 mmol of iron (III) acetylacetonate, 100 mmol of oleic acid, 112 mmol of oleyl amine, and 72 ml of 1-octadecene are mixed in a 250 ml flask. The reaction mixture is heated to 110 °C and kept under vacuum for 2 h. Then, the temperature is increased to 300 °C at a rate of 10 °C/min. After 2 h, the reaction mixture is cooled down to the room temperature and zinc ferrite NCs are precipitated by adding isopropanol. Zinc ferrite NCs are redispersed in hexane and washed further using isopropanol three times. The ratio between zinc and iron is measured by inductive coupling plasma optical emission spectrometry (ICP-OES). By increasing the heating rate to 11.7 and 15 °C/min, the size of zinc ferrite NCs can be increased to 10.1 and 12.3 nm, respectively.

C. Synthesis of iron oxide nanocrystals and $Zn_{0.1}Fe_{2.9}O_4$ nanocrystals

For the synthesis of 7.8 nm iron oxide NCs, 12 mmol of iron (III) acetylacetonate, 100 mmol of oleic acid, 112 mmol of oleyl amine, and 72 ml of 1-octadecene are mixed in a 250 ml flask. The reaction mixture is heated to 110 °C and kept under vacuum for 2 h. Then, the temperature is increased to 300 °C at a rate of 10 °C/min. After 1 h, the reaction mixture is cooled down to the room temperature, and iron oxide NCs are precipitated by adding isopropanol. Iron oxide NCs are redispersed in hexane and washed further

using isopropanol for three times. By increasing the amount of iron (III) acetylacetonate from 12 mmol to 15 mmol and 18 mmol, 9.3 nm and 12.8 nm iron oxide NCs could be obtained, respectively. To synthesize 7.4 nm $Zn_{0.1}Fe_{2.9}O_4$ NCs, 0.5 mmol of Zn (II) acetylacetonate is added into the same reaction mixture for 7.8 nm iron oxide NC synthesis. For larger sizes of NCs, the amount of Zn (II) acetylacetonate is increased to 0.63 mmol and 0.75 mmol for 10.2 nm and 13.8 nm $Zn_{0.1}Fe_{2.9}O_4$ NCs, respectively.

D. Structural characterization of ferrite nanocrystals

Transmission electron microscopy analysis is performed by using JEM-1400 microscope. Small-angle X-ray scattering data are collected at the Multi-Angle X-ray Scattering Facility at the University of Pennsylvania. Small-angle X-ray scattering data are further analyzed using Datasqueeze software.⁶³ Wide-angle X-ray scattering data are performed by using a Rigaku Smartlab high-resolution diffractometer with Cu K α radiation ($\lambda = 1.5416 \text{ \AA}$) from 20° to 80°.

E. Magnetic property characterizations of nanocrystals

1. Direct current magnetic characterization

The direct current magnetic characterizations of magnetic NCs are done by using a Superconductive Quantum Interference Device (SQUID) magnetometer with reciprocating sample option (Quantum Design MPMS-XL 7T). The hysteresis curves of magnetic NCs are measured at 300 K and 15 K from 3 T to -3 T.

2. Magnetic permeability measurement of NCs

Relative magnetic permeability of magnetic NCs is measured by using 4395A Agilent Network Analyzer and 16454A Agilent Magnetic Material Test Fixture. NCs dispersed in hexane are deposited in a toroidal shaped sample holder (8 mm of outer diameter, 3.2 mm of inner diameter, 3 mm of height, and 2.5 mm of depth) and dried. The sample holder, which is now filled with the waxy NC solid, is placed into a 16454A Agilent Magnetic Material Test Fixture. The frequency is swept from 1 MHz to 500 MHz in log frequency. The reactance and resistance of the test fixture with the sample holder are collected and then converted into the real and imaginary parts of permeability.⁵⁹ Every NC sample is averaged from three separate batches of reactions, which were prepared under the same reaction conditions.

3. Preparation of solenoid inductor

To prepare solenoid inductor with 12.3 nm $Zn_{0.25}Fe_{2.75}O_4$ NCs, a tube made of polyolefin, which contracts if heated to above 90 °C, is used. This tube has 10.9 mm of length and 3.4 mm of diameter. One of the ends is closed and the other end is open. The tube is filled with 12.3 nm $Zn_{0.25}Fe_{2.75}O_4$ NCs by simple drop casting process. After the tube is completely filled with the NCs, the open end is also sealed by melting the polyolefin. Then, the tube is heated by a heat gun to induce contraction, which increases the filling factor of the

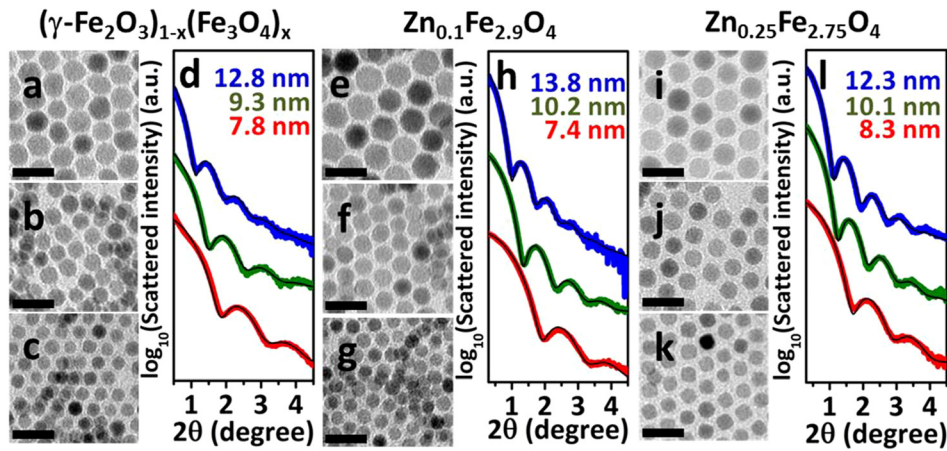


FIG. 1. Transmission electron microscope (TEM) images of (a) 12.8 nm, (b) 9.3 nm, and (c) 7.8 nm $(\gamma\text{-Fe}_2\text{O}_3)_{1-x}(\text{Fe}_3\text{O}_4)_x$ NCs, and (d) their small angle x-ray scattering (SAXS) data. The TEM images of (e) 13.8 nm, (f) 10.2 nm, and (g) 7.4 nm $\text{Zn}_{0.1}\text{Fe}_{2.9}\text{O}_4$ NCs and (h) their SAXS data. The TEM images of (i) 12.3 nm, (j) 10.1 nm, and (k) 8.3 nm $\text{Zn}_{0.25}\text{Fe}_{2.75}\text{O}_4$ NCs and (l) their SAXS data. The scale bars represent 20 nm.

NCs. After the contraction, the final diameter became 3.1 mm. Then, a seed metal layer is wound around the tube for 10 times and electroplated.

4. Inductance, resistance, and quality factor measurement of toroidal and solenoid inductors

The characterization of toroidal and solenoid inductors are done by using Agilent 4395A Agilent network analyzer and 43961A RF impedance test kit. An inductor is connected to the 43961A RF impedance test kit and its inductance and resistance are measured. The quality factor (Q) is calculated by using the equation, $Q = 2\pi fL/R$, where f is frequency, L is the inductance of the inductor, and R is the resistance of the inductor. The frequency is swept from 1 to 100 MHz in log frequency.

III. RESULTS AND DISCUSSION

Zinc ferrite NCs are synthesized through the high temperature decomposition process by modifying a previously reported method (Experimental Methods B).⁶⁴ To investigate the zinc doping level dependence of magnetic permeability, iron oxide NCs and $\text{Zn}_{0.1}\text{Fe}_{2.9}\text{O}_4$ NCs are synthesized as well. In Fig. 1, the transmission electron microscope (TEM) images of chemically synthesized ferrite NCs with various sizes and compositions are presented. Each size represents small, medium, and large NCs, and each composition represents zero, small (0.03), and large (0.09) Zn to Fe ratio. The monodispersity of NCs is observed by small angle x-ray scattering patterns (SAXS) and TEM images. The size distribution is narrow ranging from 7.3% to 9.7% by SAXS fitting simulation⁶³ and from 4.4% to 6.9% by TEM images (Table I). It is worth noting that the size distribution improves as the Zn to

Fe ratio increases. Wide angle x-ray scattering data (Fig. 2) confirms that all the samples possess spinel crystal structure (space group $Fd\bar{3}m$, No. 227). These structural analysis data indicate that the NCs are suitable subjects to study the size and Zn doping level dependence of the magnetic permeability of ferrite NCs. Note that as-synthesized iron oxide nanoparticles are a mixture of maghemite ($\gamma\text{-Fe}_2\text{O}_3$) and magnetite (Fe_3O_4) and tend to have more of the magnetite phase as their size increases.^{17,57} These two phases share the same crystal structure (spinel) but maghemite contains only of Fe^{3+} whereas magnetite possesses both Fe^{2+} and Fe^{3+} . The exact analysis of the ratio between two different phases is out of the scope of this study. Thus, the “iron oxide NCs” indicate “ $(\gamma\text{-Fe}_2\text{O}_3)_{1-x}(\text{Fe}_3\text{O}_4)_x$ ” throughout this study.

The superparamagnetism of zinc ferrite NCs is observed in dc magnetic characterization with SQUID magnetometry. The hysteresis curves (Figs. 3(a)–3(c)) at 300 K show zero coercivity in all samples, which is the typical feature of superparamagnetism.²⁷ The saturation magnetization increases with the size and zinc doping level of NCs as observed in Fig. 3(d) and Table II, which is consistent with the previously reported results.^{17,60,65} For example, the saturation magnetization of 7.8 nm iron oxide NCs is 79.6 emu/g of Fe, while that of 12.3 nm $\text{Zn}_{0.25}\text{Fe}_{2.75}\text{O}_4$ is 107.0 emu/g of Fe. Zinc ferrite NCs possess a spinel structure (AB_2O_4), which is same as the structure of magnetite (Fe_3O_4) and maghemite ($\gamma\text{-Fe}_2\text{O}_3$). Zn^{2+} prefers to occupy tetrahedral A sites over octahedral B sites. As Zn^{2+} has no net orbital angular momentum, its replacement of Fe^{3+} , which also has quenched zero orbital angular momentum, does not significantly affect the magnetocrystalline anisotropy energy. Thus, the anisotropy energy of zinc ferrite is similar to that of maghemite.⁶⁶ This is reflected in the 15 K coercivities (H_c) (Fig. 4 and Table II); when the compositions

TABLE I. The average size of ferrite NCs measured by SAXS simulation and TEM images. The numbers in the brackets indicate the size deviations.

	$(\gamma\text{-Fe}_2\text{O}_3)_{1-x}(\text{Fe}_3\text{O}_4)_x$		$\text{Zn}_{0.1}\text{Fe}_{2.9}\text{O}_4$		$\text{Zn}_{0.25}\text{Fe}_{2.75}\text{O}_4$	
	Size by SAXS	Size by TEM	Size by SAXS	Size by TEM	Size by SAXS	Size by TEM
Small	7.8 nm (9.7%)	6.1 nm (6.9%)	7.4 nm (9.2%)	6.3 nm (6.6%)	8.3 nm (8.7%)	7.3 nm (5.8%)
Medium	9.3 nm (8.8%)	7.7 nm (6.3%)	10.2 nm (7.6%)	8.5 nm (5.6%)	10.1 nm (7.7%)	8.5 nm (4.4%)
Large	12.8 nm (8.6%)	10.2 nm (6.3%)	13.8 nm (8.0%)	11.7 nm (5.5%)	12.3 nm (7.5%)	10.5 nm (4.8%)

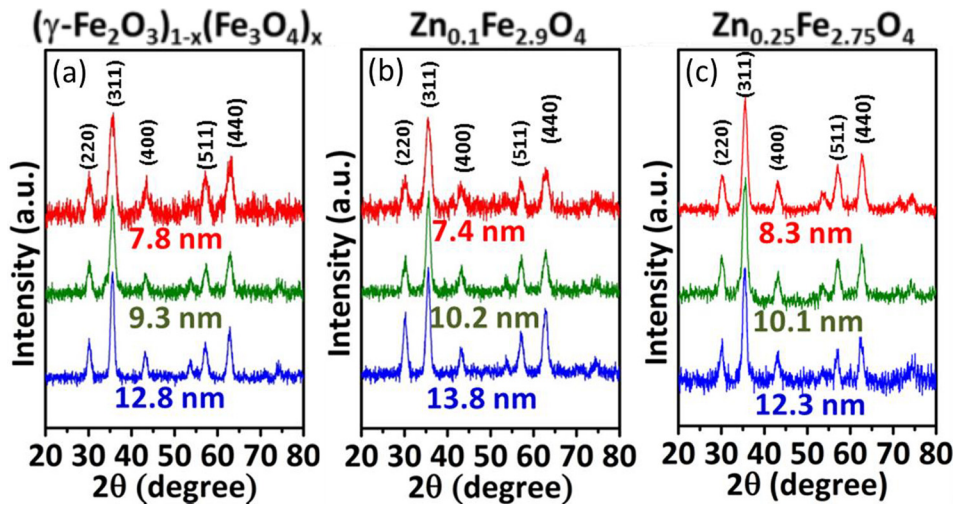


FIG. 2. The wide angle x-ray scattering data of (a) $(\gamma\text{-Fe}_2\text{O}_3)_{1-x}(\text{Fe}_3\text{O}_4)_x$ NCs, (b) $\text{Zn}_{0.1}\text{Fe}_{2.9}\text{O}_4$ NCs, and (c) $\text{Zn}_{0.25}\text{Fe}_{2.75}\text{O}_4$ NCs.

are same, the coercivity increases with the size of the NCs, but there is no systematic correlation between the composition and H_c . In contrast, doping Zn^{2+} raises the saturation magnetization.⁶⁷ The magnetism of spinel structure materials is based on ferrimagnetism whose magnetic moment comes from the difference between the magnetic moment located at two B sites and one A site due to antiparallel alignment of spins in each site.⁶⁸ As Zn^{2+} has no unpaired electrons and it prefers to occupy the A site (normal spinel structure), Zn^{2+} doped iron oxide NCs possess higher saturation magnetization than magnetite or maghemite.^{60,68} Therefore, by introducing Zn^{2+} , it should be possible to enhance the ac magnetic permeability of NCs with the increased saturation magnetization and low magnetocrystalline anisotropy energy. This explains why zinc ferrite NCs can be a good candidate for inductor cores due to the promise of low energy loss at radio frequencies. In Fig. 3(d), in general, the saturation magnetization increases with the size and Zn doping level, but the difference in smallest samples is not as apparent as in larger sizes due to the higher

surface to volume ratio of smaller NCs, which possess more disordered surface spins.⁶⁹

The ac magnetic characterization of zinc ferrite NCs is performed in a one-turn inductor model system⁷⁰ and summarized in Fig. 5. In Figs. 5(a)–5(c), the real part of the relative magnetic permeability (μ_r') curves of iron oxide, $\text{Zn}_{0.1}\text{Fe}_{2.9}\text{O}_4$, and $\text{Zn}_{0.25}\text{Fe}_{2.75}\text{O}_4$ are presented. This term is the in-phase value of the relative magnetic permeability and related to how much the material can increase the magnetic flux density in itself, that is, the larger the μ_r' , the higher the magnetic flux density.⁷¹ The result shows that μ_r' increases as the size and Zn doping level of NCs increase. This can be attributed to the increased domain size and reduced surface area of larger NCs, which results in larger magnetic moments of NCs (Fig. 3(d)). However, it is worth noting that μ_r' is not linearly proportional to the saturation magnetization value. For example, while the saturation magnetization of 12.3 nm $\text{Zn}_{0.25}\text{Fe}_{2.75}\text{O}_4$ is 30% larger than that of 12.8 nm iron oxide NCs, μ_r' is almost 60% larger, which indicates the

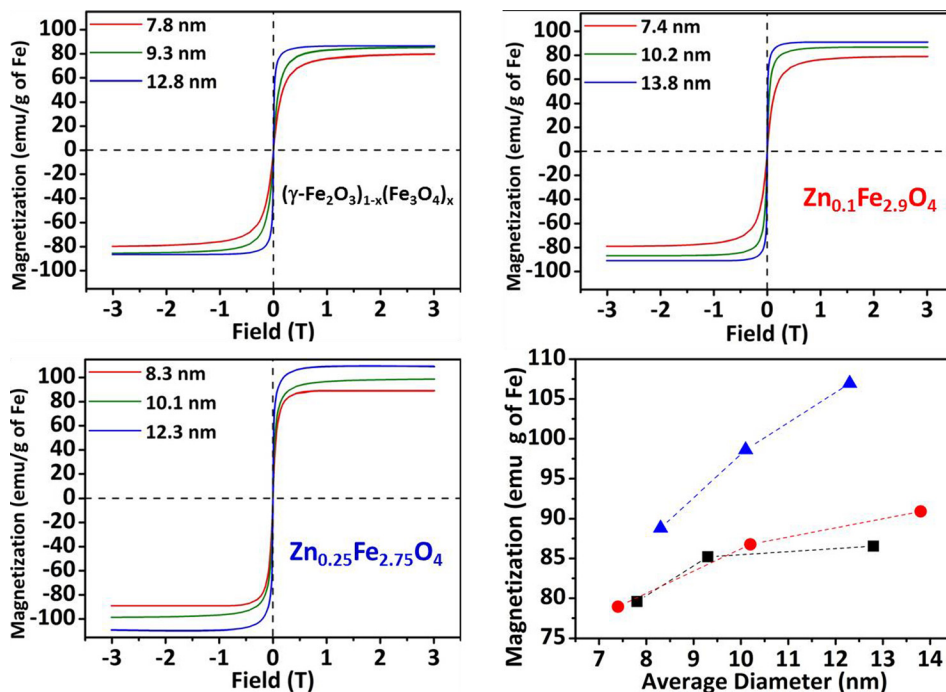


FIG. 3. 300 K hysteresis curves of (a) iron oxide NCs, (b) $\text{Zn}_{0.1}\text{Fe}_{2.9}\text{O}_4$ NCs, and (c) $\text{Zn}_{0.25}\text{Fe}_{2.75}\text{O}_4$ NCs. (d) Saturation magnetization vs NC diameter curves of $(\gamma\text{-Fe}_2\text{O}_3)_{1-x}(\text{Fe}_3\text{O}_4)_x$ (black squares), $\text{Zn}_{0.1}\text{Fe}_{2.9}\text{O}_4$ (red circles), and $\text{Zn}_{0.25}\text{Fe}_{2.75}\text{O}_4$ (blue triangles) NCs.

TABLE II. The summary of the coercivity values of NCs at 15 K and the saturation magnetization values at 300 K. H_c is coercivity and M_s is the saturation magnetization of NCs.

$(\gamma\text{-Fe}_2\text{O}_3)_x(\text{Fe}_3\text{O}_4)_{1-x}$			$\text{Zn}_{0.1}\text{Fe}_{2.9}\text{O}_4$			$\text{Zn}_{0.25}\text{Fe}_{2.75}\text{O}_4$		
Size (nm)	H_c at 15 K (mT)	M_s at 300 K (emu/g of Fe)	Size (nm)	H_c at 15 K (mT)	M_s at 300 K (emu/g of Fe)	Size (nm)	H_c at 15 K (mT)	M_s at 300 K (emu/g of Fe)
7.8 ± 0.8	4.6	79.6	7.4 ± 0.7	5.2	78.9	8.3 ± 0.7	6.7	88.8
9.3 ± 0.8	9.8	85.2	10.2 ± 0.8	10.6	86.8	10.1 ± 0.8	8.7	98.6
12.8 ± 1.1	8.8	86.5	13.8 ± 1.1	11.6	90.9	12.3 ± 0.9	10.9	107.0

importance of the ac magnetic characterizations. Compared to the previously reported values of iron oxide NCs,^{13,17} the real part of the relative magnetic permeability of zinc ferrite NCs is much higher due to their higher magnetic moment relative to iron oxide NCs. μ_r' of 12.3 nm $\text{Zn}_{0.25}\text{Fe}_{2.75}\text{O}_4$ is stable at 18–19 up to about 20–30 MHz, and this is not significantly different from the trend of similar size iron oxide NCs and $\text{Zn}_{0.1}\text{Fe}_{2.9}\text{O}_4$ NCs, as can be seen in a normalized curve (Fig. 7(a)). Therefore, by increasing the doping level of Zn in iron oxide NCs, one can increase the magnetic flux density without significantly sacrificing the operating frequency. This enhancement is possible because the Zn^{2+} has no net angular momentum, which leads to low magnetocrystalline anisotropy of the system, as mentioned before. In the

case of small NCs in the 7–8 nm range, μ_r' tends to increase as the amount of Zn increases, but the difference is not as apparent as the difference seen between larger NCs with different Zn content due to the high surface to volume ratio. One thing that should be noted is that μ_r' of iron oxide NCs is much higher than the previously reported values. In this study, μ_r' of 12.8 nm iron oxide NCs is about 11 at 1 MHz, while the similar size of NCs show 4–5 of μ_r' in our previous study.¹⁷ Also, at 100 MHz, μ_r' of 9.3 nm iron oxide NCs show 3.5 of μ_r' in this study, but iron oxide NCs with similar size were reported to possess ~ 2 of μ_r' .¹³ The reason for this difference is still under investigation.

In Figs. 5(d)–5(f), the imaginary part of the relative magnetic permeability (μ_r'') of ferrite NCs is shown. This

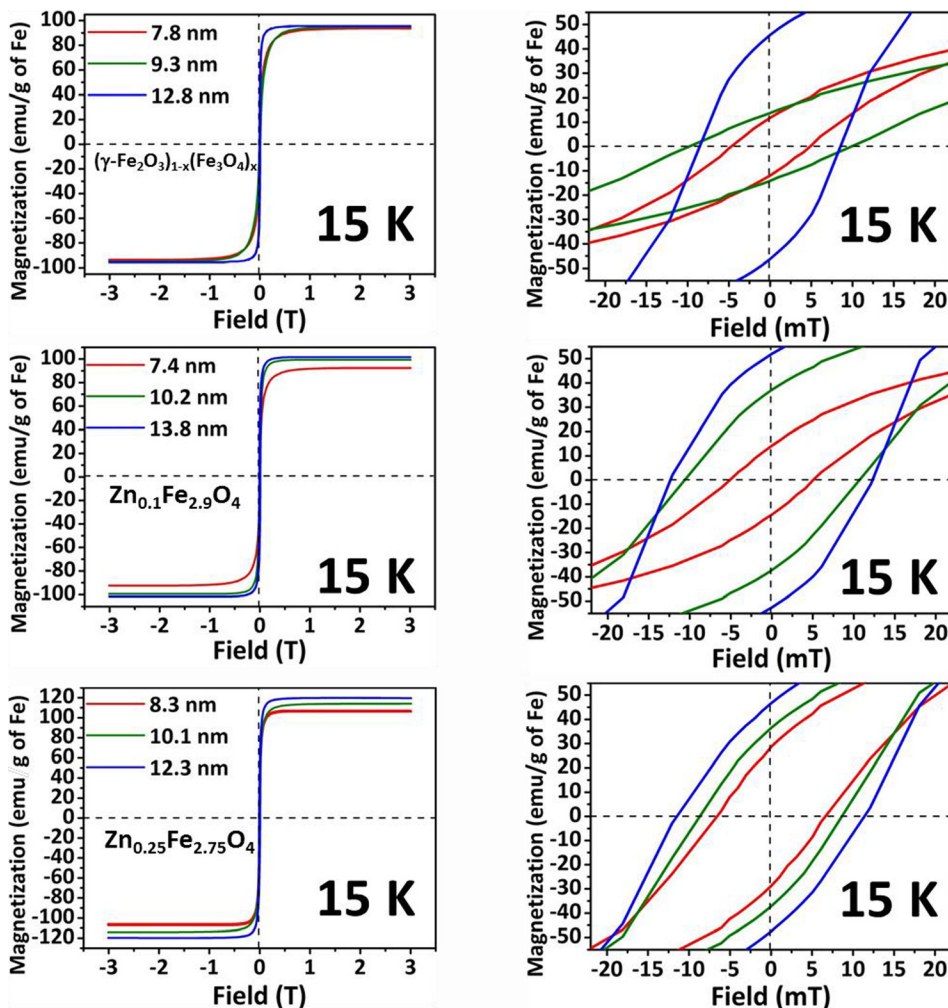


FIG. 4. The hysteresis curves of (a) $(\gamma\text{-Fe}_2\text{O}_3)_x(\text{Fe}_3\text{O}_4)_{1-x}$, (b) $\text{Zn}_{0.1}\text{Fe}_{2.9}\text{O}_4$, and (c) $\text{Zn}_{0.25}\text{Fe}_{2.75}\text{O}_4$ NCs at 15 K. The plots (d)–(f) are zoomed up plots of (a)–(c), respectively.

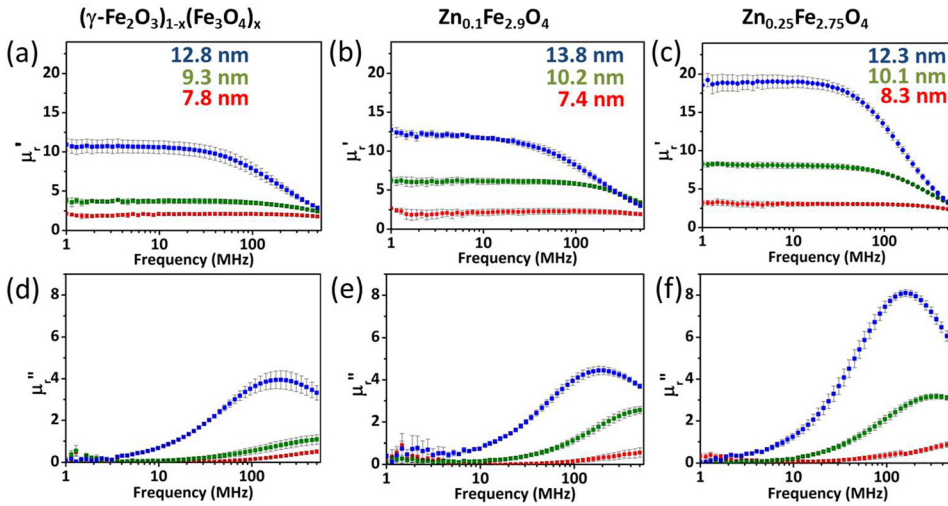


FIG. 5. The real part of relative magnetic permeability of (a) $(\gamma\text{-Fe}_2\text{O}_3)_{1-x}(\text{Fe}_3\text{O}_4)_x$ NCs, (b) $\text{Zn}_{0.1}\text{Fe}_{2.9}\text{O}_4$ NCs, and (c) $\text{Zn}_{0.25}\text{Fe}_{2.75}\text{O}_4$. The imaginary part of relative magnetic permeability of (d) $(\gamma\text{-Fe}_2\text{O}_3)_{1-x}(\text{Fe}_3\text{O}_4)_x$ NCs, (e) $\text{Zn}_{0.1}\text{Fe}_{2.9}\text{O}_4$ NCs, and (f) $\text{Zn}_{0.25}\text{Fe}_{2.75}\text{O}_4$. The relative loss tangent ($\tan \delta / \mu_r'$) of (g) $(\gamma\text{-Fe}_2\text{O}_3)_{1-x}(\text{Fe}_3\text{O}_4)_x$ NCs, (h) $\text{Zn}_{0.1}\text{Fe}_{2.9}\text{O}_4$ NCs, and (i) $\text{Zn}_{0.25}\text{Fe}_{2.75}\text{O}_4$.

term is the out-of-phase value of magnetic permeability and related to the energy loss of magnetic materials, that is, the larger the μ_r'' , the greater the energy loss. In general, the data show that μ_r'' increases as the size of NCs increases and this is consistent with previously reported studies in maghemite,¹⁷ magnetite,⁷² and manganese zinc ferrite⁷³ nanoparticles. There are two key factors that cause the increase of μ_r'' : μ_r' and δ . Since μ_r'' can be written in terms of μ_r' and δ as $\mu_r'' = \mu_r' \tan \delta$, where δ is the phase delay of the magnetic moments of materials from an external field, larger μ_r' and δ result in a higher μ_r'' . Therefore, μ_r'' increases as the size is getting larger because μ_r'' is proportional to μ_r' which is also in proportion to the size of NCs. μ_r'' is affected by the tangent loss ($\tan \delta$) as well. It is observed in Fig. 6 that the tangent loss is enhanced by the increase in the size of NCs. This can be attributed to that the larger NCs possess higher magnetic moments as can be seen in Fig. 3, leading to stronger dipolar interactions among NCs. The stronger dipolar interactions can induce more phase delay of magnetic moments from the external magnetic field.^{13,74} Therefore, considering the results of the real part of magnetic permeability and tangent loss data, it is reasonable that μ_r'' increases as the size of NCs increases.

The maximum value of μ_r'' of 12.3 nm $\text{Zn}_{0.25}\text{Fe}_{2.75}\text{O}_4$ NCs is almost double that of 12.8 nm iron oxide NCs. The

highest peak of μ_r'' can be interpreted as FMR, which occurs when the precession frequency of magnetic spins around the anisotropy field in a ferromagnetic material concurs with the external alternating field frequency. The FMR frequency decreases as the size and the amount of Zn incorporated into the NCs increases, which can be explained by Snoek's limit.⁷⁵ For a spherical nanoparticle, FMR frequency can be written as $f_r = \frac{H_k}{2\gamma}$, where f_r is the FMR frequency, γ is the gyromagnetic ratio, and H_k is the magnetic anisotropy field.⁷⁶ For cubic symmetric systems, the anisotropy field is expressed as $H_k = \frac{4K_{eff}}{30M_s}$, where K_{eff} is the effective anisotropy coefficient and M_s is the saturation magnetization. The effective anisotropy is the sum of the volume anisotropy (K_v) and the surface anisotropy (K_s). In the case of NCs, the surface anisotropy dominates the effective anisotropy constant due to their large surface area.^{65,77,78} Therefore, K_{eff} increases as the size of NCs decreases. In addition, Fig. 4 shows that M_s drops as the Zn concentration and the size of NCs decrease. As a result, due to the larger K_{eff} and smaller M_s , NC with a smaller size and Zn amount has a larger H_k , resulting a higher FMR frequency as observed in Fig. 5. For example, FMR frequency of 10.1 nm $\text{Zn}_{0.25}\text{Fe}_{2.75}\text{O}_4$ NCs is 342 MHz, whereas that of 12.3 nm $\text{Zn}_{0.25}\text{Fe}_{2.75}\text{O}_4$ NCs is 159 MHz, which indicates the effect of size on the FMR frequency. Also, FMR frequencies of 13.8 nm $\text{Zn}_{0.1}\text{Fe}_{2.9}\text{O}_4$ and 12.8 nm iron oxide NCs are at

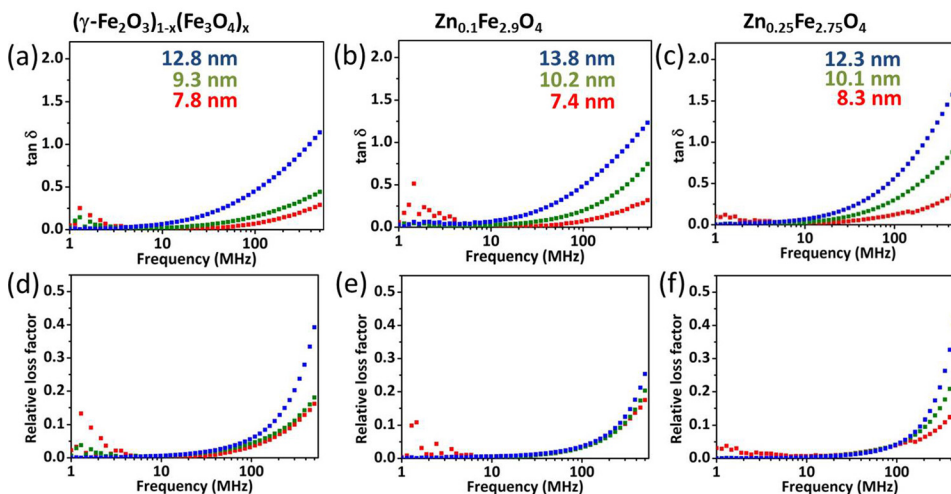


FIG. 6. The loss tangent ($\tan \delta$) of (a) $(\gamma\text{-Fe}_2\text{O}_3)_{1-x}(\text{Fe}_3\text{O}_4)_x$ NCs, (b) $\text{Zn}_{0.1}\text{Fe}_{2.9}\text{O}_4$ NCs, and (c) $\text{Zn}_{0.25}\text{Fe}_{2.75}\text{O}_4$. The relative loss tangent ($\tan \delta / \mu_r'$) of (d) $(\gamma\text{-Fe}_2\text{O}_3)_{1-x}(\text{Fe}_3\text{O}_4)_x$ NCs, (e) $\text{Zn}_{0.1}\text{Fe}_{2.9}\text{O}_4$ NCs, and (f) $\text{Zn}_{0.25}\text{Fe}_{2.75}\text{O}_4$.

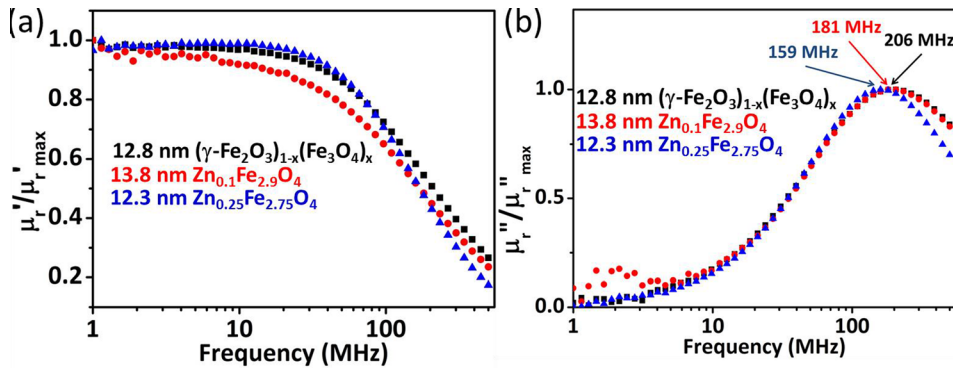


FIG. 7. The normalized curves of (a) the real part of the relative magnetic permeability and (b) the imaginary part of the relative permeability. Black squares represent 12.8 nm iron oxide NCs, red circles represent 13.8 nm $\text{Zn}_{0.1}\text{Fe}_{2.9}\text{O}_4$ NCs, and blue triangles represent 12.3 nm $\text{Zn}_{0.25}\text{Fe}_{2.75}\text{O}_4$ NCs.

181 MHz and 206 MHz, respectively, which are greater than that of 12.3 nm $\text{Zn}_{0.25}\text{Fe}_{2.75}\text{O}_4$ NCs (Fig. 7(b)). This implies that the operable frequency range for zinc ferrite NCs is more limited than that for iron oxide NCs in the radio frequency range. Even so, considering the fact that the current state of the art devices are operating at up to only a few hundred kHz,⁷⁹ our zinc ferrite NCs look like a promising option for low magnetic loss material at radio frequencies.

The efficiency of magnetic materials under an ac magnetic field can be expressed as the relative loss factor (RLF), $\tan \delta/\mu_r'$. Magnetic energy loss occurs due to the lag of internal magnetic spin directions with respect to the external field direction.⁸⁰ Therefore, it is desirable to reduce the RLF as much as possible for low energy loss applications. In Figs. 6(d)–6(f), the RLF of NCs with respect to frequency is presented. Surprisingly, the RLFs of NCs with different sizes are almost the same up to ~ 200 MHz. This suggests that zinc ferrite NCs can increase the magnetic flux density of a system at a high frequency without suffering from energy loss compared to iron oxide NCs. Also, as observed in Fig. 8, it is notable that the RLF value is in the range between 10^{-4} and 10^{-2} up to 30 MHz for 12.3 nm $\text{Zn}_{0.25}\text{Fe}_{2.75}\text{O}_4$ NCs. Also, compared to iron oxide NCs and $\text{Zn}_{0.1}\text{Fe}_{2.9}\text{O}_4$ NCs with a similar size to 12.3 nm $\text{Zn}_{0.25}\text{Fe}_{2.75}\text{O}_4$ NCs, the RLF value does not increase or change significantly, indicating that doping Zn^{2+} into the iron oxide NCs does not cause a decrease in efficiency. Since the RLF value is still lower than those of the sintered ferrite materials,^{80,81} further investigation and optimization on the NCs are necessary to increase the energy efficiency.

As a proof of concept, we have incorporated our NCs into inductors through a drop casting process. Briefly, a toroidal sample holder (8 mm of outer diameter, 3.2 mm of inner diameter, 3 mm of height, and 2.5 mm of depth) prepared by machining is filled with 12.3 nm $\text{Zn}_{0.25}\text{Fe}_{2.75}\text{O}_4$ NCs and covered with an epoxy shield. Then, a seed metal layer forming an inductor structure is wound around the sample holder and electroplated. Note that the proposed micro-machining process is not limited by the toroid shape. Fig. 9(a) shows a photograph of the toroidal inductor with zinc ferrite NC core. A solenoid inductor (Fig. 9(e)) is also fabricated and characterized, which demonstrates the flexibility of the NCs as inductor cores. The fabricated inductors are electrically characterized using an Agilent 4395A impedance analyzer in terms of inductance, resistance, and quality factor

as a function of frequency and compared with an air-core inductor, as shown in Fig. 9. An average inductance of approximately 200 nH for the toroidal inductor is measured in the frequency range of 1 to 100 MHz, as shown in Fig. 9(b). In a 10 turn solenoid inductor with NC core, about 440–450 nH inductance is observed to be stable up to 40–50 MHz (Fig. 9(f)). At higher frequencies, a resonant behavior is shown in both geometries. The toroidal inductor resistance, shown in Fig. 9(c), measures approximately 0.05 Ω at 1 MHz and slowly increased as the frequency goes up. The quality factors of the toroidal inductor (Fig. 9(d)) and solenoid inductor (Fig. 9(h)) with NC core are observed to be higher than those of air core inductors with the same geometries in the frequency ranges of 1–5 MHz and 1–9 MHz with the values over 15 and 20, respectively. The quality factors reach maximum values of 28.6 at 1.3 MHz for the toroidal inductor and 44.2 at 1.7 MHz for the solenoid inductor, indicating that the 12.3 nm $\text{Zn}_{0.25}\text{Fe}_{2.75}\text{O}_4$ NCs are energy efficient materials. The SEM images (Fig. 10) of the cross-section of the solenoid inductor show that the size/morphology of the NCs maintains their original form after the deposition into the inductor structure. In addition, the SEM image in Fig. 10(b) indicates the highly ordered and packed microstructure of the NCs in the inductor core. This encourages the use of NCs as inductor cores because the high packing density is important to utilize NCs as magnetic core materials.

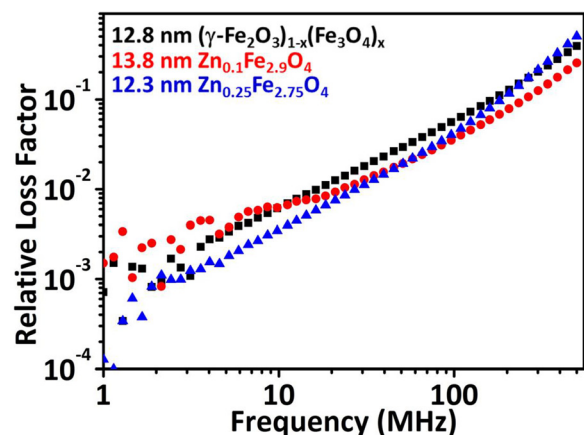


FIG. 8. The relative loss factor of 12.8 nm iron oxide NCs (black squares), 13.8 nm $\text{Zn}_{0.1}\text{Fe}_{2.9}\text{O}_4$ NCs (red circles), and 12.3 nm $\text{Zn}_{0.25}\text{Fe}_{2.75}\text{O}_4$ NCs (blue triangles) from 1 MHz to 500 MHz with y-axis in log.

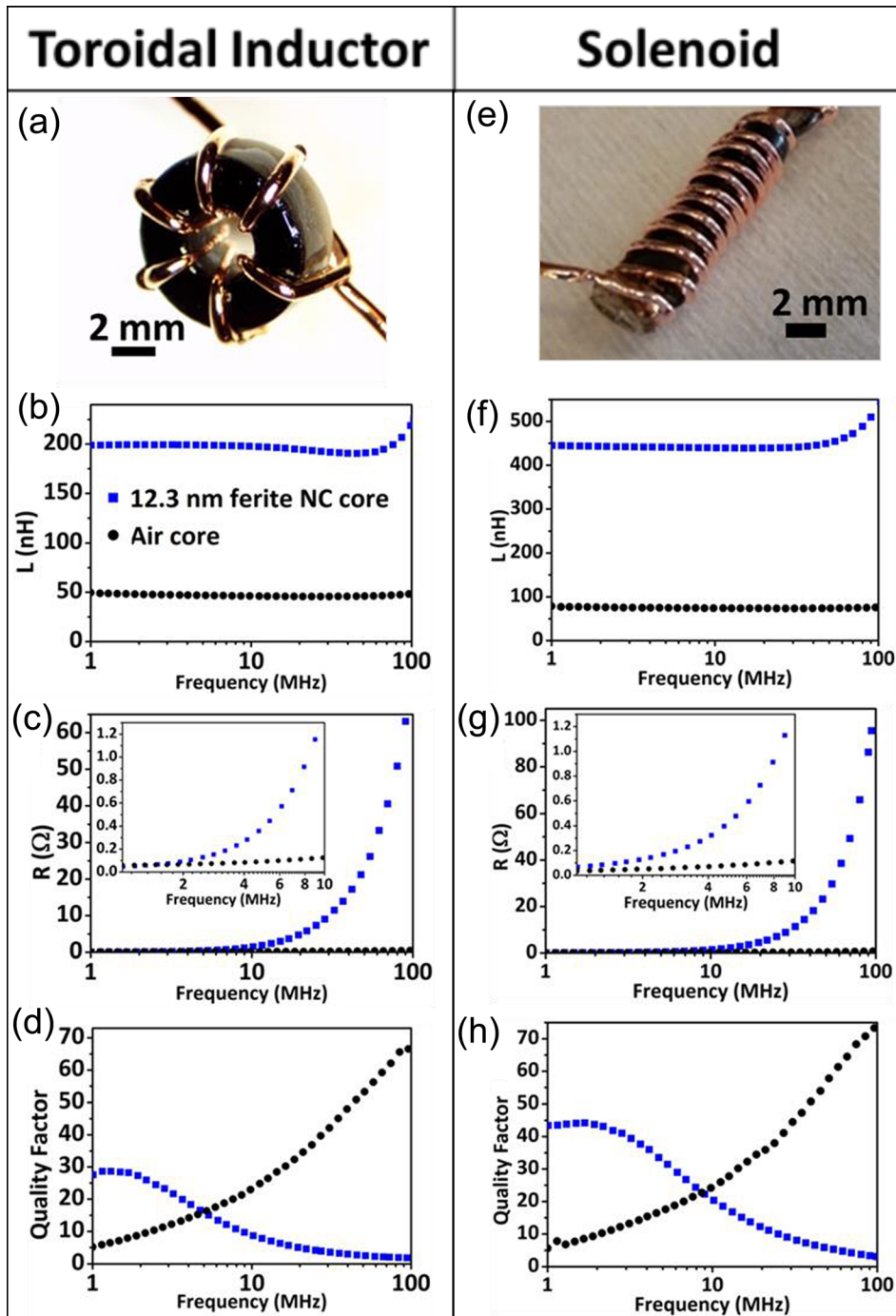


FIG. 9. (a) A photograph image of 6-turn toroidal inductor, (b) inductance, (c) resistance, and (d) quality factor. (e) A photograph image of 10-turn solenoid inductor, (f) inductance, (g) resistance, and (h) quality factor of the NC core solenoid inductor. Black dots represent the inductance, resistance, and quality factor of the air-core inductors with the same geometries. The insets in (c) and (g) are the enlarged images of the resistance curve from 1 MHz to 10 MHz.

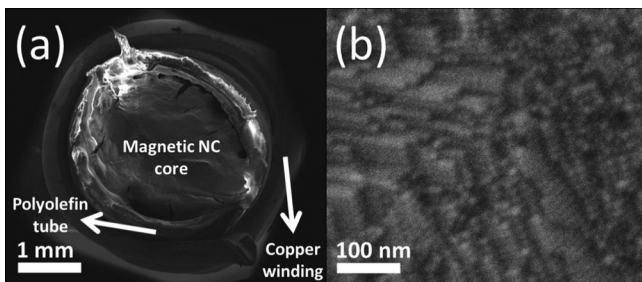


FIG. 10. (a) Scanning electron microscope image of the cross section of the solenoid inductor and (b) the high magnification images of the solenoid inductor core with 12.3 nm $\text{Zn}_{0.25}\text{Fe}_{2.75}\text{O}_4$ NCs.

IV. CONCLUSION

In summary, we synthesize nonstoichiometric zinc ferrite NCs with tunable magnetic permeability that depends on the size and Zn doping level. We observe that iron oxide NCs with higher Zn concentration and larger sizes possess higher μ_r' , but also a higher imaginary part of relative magnetic permeability. The real part of the relative magnetic permeability of 12.3 nm $\text{Zn}_{0.25}\text{Fe}_{2.75}\text{O}_4$ is almost twice that of similar sized iron oxide NCs. Even though the FMR frequency is reduced as the Zn doping level increases, the relative loss tangent curves indicate that zinc ferrite NCs do not suffer from significant energy loss as compared to iron oxide NCs. As a proof of concept, 12.3 nm $\text{Zn}_{0.25}\text{Fe}_{2.75}\text{O}_4$ NCs,

which show the highest magnetic permeability, are used to prepare inductors through a cheap and scalable solution based deposition process. Toroidal and solenoid inductors exhibit higher quality factor than those of the air core inductors with same geometries up to 5 MHz and 8–9 MHz, respectively. Further investigation should be conducted to improve the ac magnetic properties of chemically synthesized magnetic NCs.

ACKNOWLEDGMENTS

H.S.Y., J.-K.K., M.G.A., and C.B.M. were supported by the Department of Energy's Advanced Research Projects Agency-Energy (ARPA-E) DE-AR0000123, providing primary support for the synthesis of ferrite nanocrystals; structural characterization of ferrite nanocrystals by TEM and WAXS; magnetic property characterization by SQUID magnetometry and network analyzer; and the characterization of the inductors with ferrite nanocrystal cores. T.J.P. performed microscopic analysis and small angle x-ray scattering measurement of zinc ferrite NCs under support from the Office of Naval Research Multidisciplinary University Research Initiative Award No. ONR-N00014-10-1-0942. L.M. was supported by Masters Scholar Award by the department of materials science and engineering at University of Pennsylvania. J.M.K. is grateful for the support from NSF MRSEC DMR-11-20901. C.B.M. is grateful for the support from Richard Perry University Professorship.

¹V. Skumryev, S. Stoyanov, Y. Zhang, G. Hadjipanayis, D. Givord, and J. Nogues, *Science* **423**, 19 (2003).
²S. Sun, C. B. Murray, D. Weller, L. Folks, and A. Moser, *Science* **287**, 1989 (2000).
³L. Wu, P.-O. Jubert, D. Berman, W. Imaino, A. Nelson, H. Zhu, S. Zhang, and S. Sun, *Nano Lett.* **14**, 3395 (2014).
⁴J. Chen, X. Ye, S. J. Oh, J. M. Kikkawa, C. R. Kagan, and C. B. Murray, *ACS Nano* **7**, 1478 (2013).
⁵P. Dutta, P. Dey, and T. K. Nath, *J. Appl. Phys.* **102**, 073906 (2007).
⁶L. E. Hueso, J. Rivas, F. Rivadulla, and M. A. López-Quintela, *J. Appl. Phys.* **89**, 1746 (2001).
⁷S.-F. Wang, F. Xie, and R.-F. Hu, *Sens. Actuators, B* **123**, 495 (2007).
⁸C. N. Rao, U. T. Nakate, R. J. Choudhary, and S. N. Kale, *Appl. Phys. Lett.* **103**, 151107 (2013).
⁹G. Li, V. Joshi, R. L. White, S. X. Wang, J. T. Kemp, C. Webb, R. W. Davis, and S. Sun, *J. Appl. Phys.* **93**, 7557 (2003).
¹⁰Ö. Yavuz, M. K. Ram, M. Aldissi, P. Poddar, and H. Srikanth, *Synth. Met.* **151**, 211 (2005).
¹¹J. Gass, P. Poddar, J. Almand, S. Srinath, and H. Srikanth, *Adv. Funct. Mater.* **16**, 71 (2006).
¹²Y. Li, J. Zhang, Z. Liu, M. Liu, H. Lin, and R. Che, *J. Mater. Chem. C* **2**, 5216 (2014).
¹³N.-N. Song, H.-T. Yang, H.-L. Liu, X. Ren, H.-F. Ding, X.-Q. Zhang, and Z.-H. Cheng, *Sci. Rep.* **3**, 3161 (2013).
¹⁴K. M. Chowdary and S. A. Majetich, *J. Phys. D: Appl. Phys.* **47**, 175001 (2014).
¹⁵T. Ogawa, H. Kura, R. Tate, T. Oikawa, and K. Hata, *J. Appl. Phys.* **115**, 17A512 (2014).
¹⁶H. Kura, T. Ogawa, R. Tate, K. Hata, and M. Takahashi, *J. Appl. Phys.* **111**, 07B517 (2012).
¹⁷H. Yun, X. Liu, T. Paik, D. Palanisamy, J. Kim, W. D. Vogel, A. J. Viescas, J. Chen, G. C. Papaefthymiou, J. M. Kikkawa, M. G. Allen, and C. B. Murray, *ACS Nano* **8**, 12323 (2014).
¹⁸C. Desvaux, F. Dumestre, C. Amiens, M. Respaud, P. Lecante, E. Snoeck, P. Fejes, P. Renaud, and B. Chaudret, *J. Mater. Chem.* **19**, 3268 (2009).
¹⁹C. Desvaux, C. Amiens, P. Fejes, P. Renaud, M. Respaud, P. Lecante, E. Snoeck, and B. Chaudret, *Nat. Mater.* **4**, 750 (2005).

²⁰W. Guan, M. Jin, Y. Fan, J. Chen, P. Xin, Y. Li, K. Dai, H. Zhang, T. Huang, and J. Ruan, *IEEE Trans. Magn.* **50**, 253 (2014).
²¹C. Choi, H. S. Yoo, and J. M. Oh, *Curr. Appl. Phys.* **8**, 710 (2008).
²²J. Miao, M. Dong, M. Ren, X. Wu, L. Shen, and H. Wang, *J. Appl. Phys.* **113**, 204103 (2013).
²³P. Guardia, R. D. Corato, L. Lartigue, C. Wilhelm, A. Espinosa, M. Garcia-hernandez, F. Gazeau, L. Manna, and T. Pellegrino, *ACS Nano* **6**, 3080 (2012).
²⁴R. Hergt, W. Andr, C. G. Ambly, I. Hilger, W. A. Kaiser, U. Richter, and H. Schmidt, *IEEE Trans. Magn.* **34**, 3745 (1998).
²⁵J.-H. Lee, J.-T. Jang, J.-S. Choi, S. H. Moon, S.-H. Noh, J.-W. Kim, J.-G. Kim, I.-S. Kim, K. I. Park, and J. Cheon, *Nat. Nanotechnol.* **6**, 418 (2011).
²⁶S.-H. Noh, W. Na, J.-T. Jang, J.-H. Lee, E. J. Lee, S. H. Moon, Y. Lim, J.-S. Shin, and J. Cheon, *Nano Lett.* **12**, 3716 (2012).
²⁷C. P. Bean and J. D. Livingston, *J. Appl. Phys.* **30**, S120 (1959).
²⁸M. G. Panthani, V. Akhavan, B. Goodfellow, J. P. Schmidtke, L. Dunn, A. Dodabalapur, P. F. Barbara, and B. A. Korgel, *J. Am. Chem. Soc.* **130**, 16770 (2008).
²⁹M. Nguyen, P. D. Tran, S. S. Pramana, R. L. Lee, S. K. Batabyal, N. Mathews, L. H. Wong, and M. Graetzel, *Nanoscale* **5**, 1479 (2013).
³⁰Y. Gao and M. Nagai, *Langmuir* **22**, 3936 (2006).
³¹L. Li, N. Coates, and D. Moses, *J. Am. Chem. Soc.* **132**, 22 (2010).
³²M. Mushrush, A. Facchetti, M. Lefenfeld, H. E. Katz, T. J. Marks, L. Technologies, A. V. Mountain, and M. Hill, *J. Am. Chem. Soc.* **125**, 9414 (2003).
³³C. Y. Lee, M. Y. Lin, W. H. Wu, J. Y. Wang, Y. Chou, W. F. Su, Y. F. Chen, and C. F. Lin, *Semicond. Sci. Technol.* **25**, 105008 (2010).
³⁴C. R. Kagan, D. B. Mitzi, and C. D. Dimitrakopoulos, *Science* **286**, 945 (1999).
³⁵Y. M. Park, J. Daniel, M. Heeney, and A. Salles, *Adv. Mater.* **23**, 971 (2011).
³⁶J. Wang, J. Zhang, A. K. Sundramoorthy, P. Chen, and M. B. Chan-Park, *Nanoscale* **6**, 4560 (2014).
³⁷L. Supriya and R. O. Claus, *Langmuir* **20**, 8870 (2004).
³⁸T. Sekitani, K. Zaito, Y. Noguchi, K. Ishibe, M. Takamiya, T. Sakurai, and T. Someya, *IEEE Trans. Electron Devices* **56**, 1027 (2009).
³⁹Y.-S. Hsiao, W.-T. Whang, S.-C. Wu, and K.-R. Chuang, *Thin Solid Films* **516**, 4258 (2008).
⁴⁰X. Sun, X. Peng, Y. Zheng, X. Li, and H. A. Zhang, *IEEE J. Microelectromech. Syst.* **23**, 888 (2014).
⁴¹D. Yao, C. G. Levey, R. Tian, and C. R. Sullivan, *IEEE Trans. Power Electron.* **28**, 4384 (2013).
⁴²P. J. Chen, S. Saati, R. Varma, M. S. Humayun, and Y. C. Tai, *J. Microelectromech. Syst.* **19**, 721 (2010).
⁴³E. Waffenschmidt, B. Ackermann, and M. Wille, in *Proceedings of IEEE 36th Power Electronics Specialists Conference* (2005), p. 1528.
⁴⁴H. Dong, F. Liu, C. P. Wong, Q. Song, and Z. J. Zhang, in *Proceedings of the 9th International Symposium on Advanced Packaging Materials* (2004), p. 171.
⁴⁵S. L. Ho, J. Wang, W. N. Fu, and M. Sun, *IEEE Trans. Magn.* **47**, 1522 (2011).
⁴⁶J. H. Cheong, K. L. Chan, B. Khannur, K. T. Tiew, and M. Je, *IEEE Trans. Circuits Syst.* **58**, 407 (2011).
⁴⁷W. X. Zhong, X. Liu, and S. Y. R. Hui, *IEEE Trans. Ind. Electron.* **58**, 4136 (2011).
⁴⁸B. E. Horton, S. Schweitzer, A. J. DeRouin, and K. G. Ong, *IEEE Sens. J.* **11**, 1061 (2011).
⁴⁹J. Kim, F. Herrault, X. Yu, M. Kim, R. H. Shafer, and M. G. Allen, *J. Micromech. Microeng.* **23**, 035006 (2013).
⁵⁰J. Qiu, S. Member, C. R. Sullivan, and S. Member, *IEEE Trans. Power Electron.* **27**, 4965 (2012).
⁵¹D. Hasegawa, H. Yang, T. Ogawa, and M. Takahashi, *J. Magn. Magn. Mater.* **321**, 746 (2009).
⁵²Z. Ni, J. Zhan, Q. Fang, X. Wang, S. Member, Z. Shi, Y. Yang, T. Ren, S. Member, A. Wang, Y. Cheng, J. Gao, X. Li, and C. Yang, *IEEE Trans. Electron Devices* **60**, 1427 (2013).
⁵³M. Pasquale, F. Celegato, M. Coisson, A. Magni, S. Perero, P. Kabos, V. Teppati, S. H. Han, J. Kim, and S. H. Lim, *J. Appl. Phys.* **99**, 08M303 (2006).
⁵⁴P. David and M. Heath, *J. Phys. C: Solid State Phys.* **3**, 1356 (1970).
⁵⁵H. Kura, K. Hata, T. Oikawa, M. Takahashi, and T. Ogawa, *Scr. Mater.* **76**, 65 (2014).
⁵⁶R. Ramprasad, P. Zurcher, M. Petras, M. Miller, and P. Renaud, *J. Appl. Phys.* **96**, 519 (2004).

- ⁵⁷J. Park, K. An, Y. Hwang, J.-G. Park, H.-J. Noh, J.-Y. Kim, J.-H. Park, N.-M. Hwang, and T. Hyeon, *Nat. Mater.* **3**, 891 (2004).
- ⁵⁸A. Lak, M. Kraken, F. Ludwig, A. Kornowski, D. Eberbeck, S. Sievers, F. J. Litterst, H. Weller, and M. Schilling, *Nanoscale* **5**, 12286 (2013).
- ⁵⁹R. L. Rebodos and P. J. Vikesland, *Langmuir* **26**, 16745 (2010).
- ⁶⁰Y. Yang, X. Liu, Y. Yang, W. Xiao, Z. Li, D. Xue, F. Li, and J. Ding, *J. Mater. Chem. C* **1**, 2875 (2013).
- ⁶¹C. Yao, Q. Zeng, G. F. Goya, T. Torres, J. Liu, H. Wu, M. Ge, Y. Zeng, Y. Wang, and J. Z. Jiang, *J. Phys. Chem. C* **111**, 12274 (2007).
- ⁶²A. A. Birajdar, S. E. Shirsath, R. H. Kadam, M. L. Mane, D. R. Mane, and A. R. Shitre, *J. Appl. Phys.* **112**, 053908 (2012).
- ⁶³T. R. Gordon, B. T. Diroll, T. Paik, V. V. T. Doan-Nguyen, E. A. Gaulding, and C. B. Murray, *Chem. Mater.* **27**, 2502 (2015).
- ⁶⁴S. Sun, H. Zeng, D. B. Robinson, S. Raoux, P. M. Rice, S. X. Wang, and G. Li, *J. Am. Chem. Soc.* **126**, 273 (2004).
- ⁶⁵A. Demortière, P. Panissod, B. P. Pichon, G. Pourroy, D. Guillon, B. Donnio, and S. Bégin-Colin, *Nanoscale* **3**, 225 (2011).
- ⁶⁶J. F. Hochepped, P. Bonville, and M. P. Pileni, *J. Phys. Chem. B* **104**, 905 (2000).
- ⁶⁷D. S. Mathew and R. S. Juang, *Chem. Eng. J.* **129**, 51 (2007).
- ⁶⁸E. C. Snelling and A. D. Giles, *Ferrites for Inductors and Transformers* (Research Studies Press/Wiley, Letchworth, Herts/New York, 1983).
- ⁶⁹C. Caizer and M. Stefanescu, *J. Phys. D: Appl. Phys.* **35**, 3035 (2002).
- ⁷⁰J. Shenhui, S. Member, and J. Quanxing, *IEEE Trans. Electromagn. Compat.* **47**, 651 (2005).
- ⁷¹B. D. Cullity, *Introduction to Magnetic Materials*, 2nd ed. (Wiley, Hoboken, New Jersey/IEEE Press, Piscataway, New Jersey, 2009).
- ⁷²S. van Berkum, J. T. Dee, A. P. Philipse, and B. H. Erne, *Int. J. Mol. Sci.* **14**, 10162 (2013).
- ⁷³N. E. Kazantseva, Y. I. Bespyatykh, I. Sapurina, J. Stejskal, J. Vilčáková, and P. Sáva, *J. Magn. Magn. Mater.* **301**, 155 (2006).
- ⁷⁴J. García-otero, M. Porto, J. Rivas, and A. Bunde, *Phys. Rev. Lett.* **84**, 167 (2000).
- ⁷⁵J. L. Snoek, *Nature* **160**, 90 (1947).
- ⁷⁶C. Kittel, *Phys. Rev.* **73**, 155 (1948).
- ⁷⁷S. J. Yan, L. Zhen, C. Y. Xu, J. T. Jiang, and W. Z. Shao, *J. Phys. D: Appl. Phys.* **43**, 245003 (2010).
- ⁷⁸S. P. Gubin, Y. A. Koksharov, G. B. Khomutov, and G. Y. Yurkov, *Russ. Chem. Rev.* **74**, 489 (2005).
- ⁷⁹M. Araghchini, J. Chen, V. Doan-nguyen, D. V. Harburg, D. Jin, J. Kim, M. S. Kim, S. Lim, B. Lu, D. Piedra, J. Qiu, J. Ranson, M. Sun, X. Yu, H. Yun, M. G. Allen, A. Alamo, G. Desgroseilliers, F. Herrault, J. H. Lang, C. G. Levey, C. B. Murray, D. Otten, D. J. Perreault, and C. R. Sullivan, *IEEE Trans. Power Electron.* **28**, 4182 (2013).
- ⁸⁰J. Chand, G. Kumar, P. Kumar, S. K. Sharma, M. Knobel, and M. Singh, *J. Alloys Compd.* **509**, 9638 (2011).
- ⁸¹F. Nesa, *World J. Condens. Matter Phys.* **02**, 27 (2012).